Geophys. J. Int. (1996) **127**, 156–168

Tensorial formulation of the wave equation for modelling curved interfaces

Dimitri Komatitsch,[1] Fabien Coutel[2] and Peter Mora[2]

[1] *Institut de Physique du Globe, 4 Place Jussieu, 75252 Paris, France*

[2] *Queensland University Advanced Center for Earthquake Studies, 4072 Qld, Brisbane, Australia*

Accepted 1996 May 30. Received 1996 January 22; in original form 1995 June 1

SUMMARY

Many situations of practical interest involving seismic wave modelling require curved interfaces and free-surface topography to be taken into account. Collocation methods, for instance pseudospectral or finite-difference algorithms, are attractive approaches for modelling wave propagation through these complex realistic models, particularly in view of their ease of implementation. Nonetheless, these methods formulated in Cartesian coordinates are not well suited to such models because the sharp interfaces and free surface do not coincide with grid lines. This leads to a slow convergence rate, resulting in visible artefacts such as diffractions from staircase discretizations of interfaces and the free surface. Such problems can be overcome through the use of curved grids whose lines follow sharp interfaces and whose density increases in the vicinity of these interfaces. One approach is to solve the wave equation in Cartesian coordinates by using the chain rule to express the Cartesian partial derivatives in terms of derivatives computed in the new coordinate system. However, it is more natural to solve the tensorial form of the wave equation directly in the desired curvilinear coordinate system, making use of a transformation of a square grid onto the curved grid. The tensorial approach, which is independent of the coordinate system, requires the same number of derivatives to be computed as in the Cartesian case, whereas the chain rule approach requires 25 per cent more in 2-D and 50 per cent more in 3-D. While the tensorial approach is less computationally expensive than the chain rule method, it requires more memory. Numerical tests validate the tensorial approach by comparing the results with the analytical solution of the tilted Lamb problem. Other numerical experiments demonstrate the ability of the tensorial formulation to model wave propagation in the presence of free-surface topography. Mode conversions between Rayleigh and body waves are observed when bumps on the free surface are encountered.

Key words: Rayleigh waves, seismic modelling, topography, wave equation.

INTRODUCTION

In many situations, it is important to simulate wave propagation in models containing curved interfaces and/or free-surface topography. In such cases, the use of classical collocation methods (i.e. Cartesian grid methods) has the drawback of poor convergence rates, as evidenced by visible artefacts such as diffractions from the staircase discretization of the interfaces and free surface. In the case of curved interfaces within the model, such artefacts can be reduced by careful discretization procedures that involve 'interpolation' of the model onto the Cartesian grid (e.g. Muir *et al.* 1992) albeit with convergence limitations imposed by the uniform discretization. However, for the case of a free surface with topography, there seems to be no easy way to implement the appropriate discrete boundary conditions correctly.

An approach to overcome these problems, initially introduced by Fornberg (1988) and later developed by many authors (Tessmer, Kosloff & Behle 1992; Carcione 1994; Nielsen *et al.* 1994; Hestholm & Ruud 1994; Tessmer & Kosloff 1994), is to solve the wave equation on a curved grid whose lines coincide with the interfaces. This is achieved by solving the wave equation written in Cartesian coordinates and involves first computing the spatial derivatives in the new coordinate system (curved grid) and then applying the chain rule to calculate the required Cartesian spatial derivatives. This method allows curved interfaces to be modelled but has the major drawback of being computationally more expensive

than the Cartesian method because more derivatives must be computed.

A more natural approach, which overcomes this drawback, is to solve the wave equation on the curved grid directly. This necessitates the wave equation to be written in its tensorial form, which is independent of the coordinate system. A grid transformation maps the curved grid, whose lines coincide with sharp interfaces and/or the free surface, onto a square computational grid. This enables the metric tensor, which is needed to solve the tensorial wave equation, to be computed at any point in the medium. The solution to the tensorial wave equation involves the computation of exactly the same number of derivatives as in the Cartesian case.

The grid generation process ensures that the grid lines lie on the different interfaces, so that the 'non-physical' diffractions from the staircase discretization in Cartesian grids are not present. Local grid refinement in the vicinity of the interfaces (in particular the free surface) allows the convergence rate to be improved relative to Cartesian methods. Complex domains can also be discretized using grids that are orthogonal at every point in space. This leads to a reduction in the memory requirements of the tensorial approach (the off-diagonal components of the metric tensor being equal to zero) but, as underlined by Thompson, Warsi & Mastin (1985) and Nielsen & Skovgaard (1990), orthogonality is not the key requirement for a small computational error. A much more important factor is the smoothness of the variations in the size of the grid cells, which is ensured by the grid generation process (see Appendix B).

TENSORIAL FORMULATION OF THE WAVE EQUATION

The tensorial wave equation

The wave equation is most frequently written using Cartesian coordinates. However, the introduction of a particular coordinate system is not necessary provided a 'metric' can be defined. In this case, a set of equations describing elastic wave propagation in heterogeneous media can be written that is valid at any point in space independently of the particular choice of coordinates. This choice merely specifies the components of the metric tensor g_{ij} but the equations themselves remain unchanged. For the case of an isotropic medium and assuming infinitesimal strains, the general expression of these tensorial equations (see also McConnell 1957; Brillouin 1964) is the equation for the conservation of linear momentum

$$\rho \frac{\partial^2 u_i}{\partial t^2} = \nabla_j \sigma_i{}^j + \varphi_i, \tag{1}$$

the strain–displacement relation (under the infinitesimal strain approximation)

$$\varepsilon_{ij} = \frac{1}{2}(\nabla_i u_j + \nabla_j u_i), \tag{2}$$

and the isotropic stress–strain relation, or Hooke's law,

$$\sigma_i{}^j = \lambda g_i{}^j \varepsilon_k{}^k + 2\mu \varepsilon_i{}^j, \tag{3}$$

where the covariant derivative ∇_m of a tensor $T_{ij\ldots}{}^{kl\ldots}$ has the general expression

$$\begin{aligned}\nabla_m T_{ij\ldots}{}^{kl\ldots} &= \partial_m T_{ij\ldots}{}^{kl\ldots} \\ &\quad - \Gamma_{mi}{}^s T_{sj\ldots}{}^{kl\ldots} - \Gamma_{mj}{}^s T_{is\ldots}{}^{kl\ldots} - \ldots \\ &\quad + \Gamma_{ms}{}^k T_{ij\ldots}{}^{sl\ldots} + \Gamma_{ms}{}^l T_{ij\ldots}{}^{ks\ldots} + \ldots .\end{aligned} \tag{4}$$

For the purpose of numerical computations, we rewrite the wave equation in velocity–stress formulation (Virieux 1986). In 2-D, the linear momentum conservation is then

$$\begin{aligned}\rho \frac{\partial v_\xi}{\partial t} &= \nabla_\xi \sigma_\xi{}^\xi + \nabla_\eta \sigma_\xi{}^\eta + \varphi_\xi \\ &= \partial_\xi \sigma_\xi{}^\xi + \partial_\eta \sigma_\xi{}^\eta + \Gamma_{\eta\xi}{}^\eta \sigma_\xi{}^\xi + \Gamma_{\eta\eta}{}^\eta \sigma_\xi{}^\eta - \Gamma_{\xi\xi}{}^\eta \sigma_\eta{}^\xi \\ &\quad - \Gamma_{\eta\xi}{}^\eta \sigma_\eta{}^\eta + \varphi_\xi . \\ \rho \frac{\partial v_\eta}{\partial t} &= \nabla_\xi \sigma_\eta{}^\xi + \nabla_\eta \sigma_\eta{}^\eta + \varphi_\eta \\ &= \partial_\xi \sigma_\eta{}^\xi + \partial_\eta \sigma_\eta{}^\eta + \Gamma_{\xi\xi}{}^\xi \sigma_\eta{}^\xi + \Gamma_{\xi\eta}{}^\xi \sigma_\eta{}^\eta - \Gamma_{\xi\eta}{}^\xi \sigma_\xi{}^\xi \\ &\quad - \Gamma_{\eta\eta}{}^\xi \sigma_\xi{}^\eta + \varphi_\eta ;\end{aligned} \tag{5}$$

the isotropic stress–strain relation is

$$\begin{aligned}\dot\sigma_\xi{}^\xi &= (\lambda + 2\mu)\dot\varepsilon_\xi{}^\xi + \lambda \dot\varepsilon_\eta{}^\eta , \\ \dot\sigma_\eta{}^\eta &= \lambda \dot\varepsilon_\xi{}^\xi + (\lambda + 2\mu)\dot\varepsilon_\eta{}^\eta , \\ \dot\sigma_\xi{}^\eta &= 2\mu \dot\varepsilon_\xi{}^\eta , \\ \dot\sigma_\eta{}^\xi &= 2\mu \dot\varepsilon_\eta{}^\xi ;\end{aligned} \tag{6}$$

the strain–velocity relation is

$$\begin{aligned}\dot\varepsilon_{\xi\xi} &= \nabla_\xi v_\xi = \partial_\xi v_\xi - \Gamma_{\xi\xi}{}^\xi v_\xi - \Gamma_{\xi\xi}{}^\eta v_\eta , \\ \dot\varepsilon_{\eta\eta} &= \nabla_\eta v_\eta = \partial_\eta v_\eta - \Gamma_{\eta\eta}{}^\xi v_\xi - \Gamma_{\eta\eta}{}^\eta v_\eta , \\ \dot\varepsilon_{\xi\eta} &= \dot\varepsilon_{\eta\xi} = \frac{1}{2}(\nabla_\xi v_\eta + \nabla_\eta v_\xi) = \frac{1}{2}(\partial_\xi v_\eta + \partial_\eta v_\xi) - \Gamma_{\xi\eta}{}^\xi v_\xi - \Gamma_{\xi\eta}{}^\eta v_\eta ;\end{aligned} \tag{7}$$

and the strain tensor transformation between covariant and mixed formulation is

$$\begin{aligned}\dot\varepsilon_\xi{}^\xi &= g^{\xi\xi}\dot\varepsilon_{\xi\xi} + g^{\eta\xi}\dot\varepsilon_{\xi\eta} , \\ \dot\varepsilon_\eta{}^\eta &= g^{\xi\eta}\dot\varepsilon_{\eta\xi} + g^{\eta\eta}\dot\varepsilon_{\eta\eta} , \\ \dot\varepsilon_\xi{}^\eta &= g^{\xi\eta}\dot\varepsilon_{\xi\xi} + g^{\eta\eta}\dot\varepsilon_{\xi\eta} , \\ \dot\varepsilon_\eta{}^\xi &= g^{\xi\xi}\dot\varepsilon_{\eta\xi} + g^{\eta\xi}\dot\varepsilon_{\eta\eta} .\end{aligned} \tag{8}$$

In the above set of equations, ξ and η are the curvilinear coordinates, λ and μ are the Lamé parameters of the elastic medium, ρ is the density, v_i denotes the covariant components of the velocity vector, φ_i is the covariant source term, ε_{ij} is the covariant strain tensor, $\varepsilon_i{}^j$ is the mixed strain tensor (i.e. one covariant and one contravariant index) and $\sigma_i{}^j$ is the mixed stress tensor. A dot over a tensor denotes time differentiation. $\Gamma_{ij}{}^k$ is the affine connection (Christoffel symbols of the second kind), which can be derived from the metric tensor using

$$\Gamma_{ij}{}^k = \frac{1}{2} g^{km}(\partial_i g_{jm} + \partial_j g_{im} - \partial_m g_{ij}). \tag{9}$$

Note that we use Einstein's summation convention of implicit summation over an index repeated as a subscript and a superscript. The symbols ∇_ξ and ∇_η stand for the so-called covariant derivative, which is equal to the partial derivative plus a sum of the components of the field itself multiplied by the Christoffel symbols. Information about the coordinate system is contained in the metric, with g_{ij} denoting the metric tensor in covariant components and g^{ij} the metric tensor

in contravariant components. Appendix A provides a brief review of the essential rules of covariant and contravariant formulations of tensors.

Assuming it is possible to define a coordinate system that matches naturally onto the physical space (i.e. one in which given axis ordinates coincide with geological interfaces and surfaces), the above set of equations can be applied to solve the wave equation directly in this 'geological' coordinate system. This corresponds to solving the wave equation in a square computational grid $(\xi, \eta) \in [-1, 1] \times [-1, 1]$ that maps onto the physical space (x, z) through a given transformation. In contrast to the chain rule method, where the wave equation in a Cartesian coordinate system (i.e. written in terms of velocity components v_x and v_z and stress components σ_{xx}, σ_{zz} and σ_{xz} for the 2-D case) is solved using spatial derivatives calculated in the curvilinear domain, the tensorial method directly solves the wave equation in the curvilinear domain (i.e. the equation written in terms of velocity components v_ξ and v_η and stress components $\sigma_{\xi\xi}$, $\sigma_{\eta\eta}$ and $\sigma_{\xi\eta}$) using spatial derivatives calculated in the same curvilinear domain.

Computational cost

While the tensorial approach is more philosophically satisfying than the chain rule approach because the equations are written in the same curvilinear coordinate system as where computations are performed, the relative costs of the two approaches have to be analysed under similar assumptions. A cost comparison between methods is difficult due to a multitude of possible implementations. In the following indicative analysis, relatively similar implementations are assumed in which time-independent coefficients are stored rather than recomputed at every time step (e.g. $\Gamma_{ij}^{\ k}$ in the case of the tensorial approach and $\partial\xi_m/\partial x_i$ in the case of the chain rule method).

The computational cost of a numerical approach to solve the wave equation directly depends mainly on the number of spatial derivatives required by the method, denoted by n_∂ (assuming a precise discrete derivative operator is used—for example a pseudospectral operator or a finite-difference operator of length ≥ 4). Consequently, we will use the number of spatial derivatives required by an approach as an indicative measure of the computational cost, i.e.

$$\textit{Computational cost} \sim \textit{constant} \times n_\partial(N), \tag{10}$$

where N denotes the number of spatial dimensions.

For the tensorial formulation, the number of spatial derivatives required to compute the divergence of the stress is N^2, and the number required to calculate the strain from the displacement is also N^2, giving a total of

$$n_\partial^{\text{tensorial}} = 2N^2 \tag{11}$$

discrete spatial derivative computations. This is identical to the number of spatial derivatives required by the Cartesian approach, which is a special case of the tensorial approach with $g_{ij} = \delta_{ij} = \textit{constant}$, simply meaning that all the Christoffel symbols equal zero.

The chain rule approach calculates the Cartesian derivatives in terms of the derivatives in the computational domain as

$$\frac{\partial f}{\partial x_i} = \frac{\partial f}{\partial \xi_m}\frac{\partial \xi_m}{\partial x_i}, \tag{12}$$

where ξ_m denotes the coordinates in the computational domain and f the field being differentiated. The divergence of stress is therefore calculated as

$$\frac{\partial \sigma_{ij}}{\partial x_j} = \frac{\partial \sigma_{ij}}{\partial \xi_m}\frac{\partial \xi_m}{\partial x_j}, \tag{13}$$

which involves the computation of $N^2 \times (N+1)/2$ independent spatial derivatives. In the case of the strain calculation using the chain rule, the most efficient way in terms of computational cost is to compute and store the N^2 spatial derivatives $\partial u_i/\partial \xi_m$ and subsequently apply eq. (12). Consequently, the total number of discrete derivatives that must be computed in the chain rule approach is

$$n_\partial^{\text{chain}} = N^2\left(\frac{3}{2} + \frac{N}{2}\right). \tag{14}$$

Therefore, the additional cost of the chain rule approach relative to the tensorial approach is

$$\frac{\textit{Cost chain rule}}{\textit{Cost tensorial}} \sim \frac{n_\partial^{\text{chain}}}{n_\partial^{\text{tensorial}}} = \frac{3}{4} + \frac{N}{4} \equiv \begin{cases} 125 \text{ per cent}, & N = 2, \\ 150 \text{ per cent}, & N = 3. \end{cases} \tag{15}$$

If only the horizontal lines were curved, while keeping purely vertical grid lines, as is often done in the chain rule method to reduce the cost when curved grids are generated for smooth enough topographies, the additional cost of the chain rule relative to the tensorial approach would be of 112.5 per cent in 2-D and 122.2 per cent in 3-D, due to the fact that some of the $\partial\xi_m/\partial x_i$ would then be equal to zero.

While the tensorial formulation requires a computational effort similar to the Cartesian case, additional memory is required to store the metric g^{ij} and connection $\Gamma_{ij}^{\ k}$. Recalling that the metric tensor is symmetric and that the connection is symmetric in the lower indices, the memory requirement is $N(N+1)/2$ fields for the metric and $N^2(N+1)/2$ fields for the connection. This requirement applies to the general case when g^{ij} has no zero components. We denote the extra memory requirement of the tensorial approach to store the metric and connection by

$$\Delta M^{\text{tensorial}} = \frac{N(N+1)^2}{2}. \tag{16}$$

Similarly, the chain rule approach requires additional memory relative to the Cartesian case to store the N^2 fields $\partial\xi_m/\partial x_i$, so

$$\Delta M^{\text{chain}} = N^2. \tag{17}$$

This is less than the additional memory required by the tensorial method, the difference between the two approaches being

$$\Delta M^{\text{tensorial}} - \Delta M^{\text{chain}} = \frac{N(N^2+1)}{2} = \begin{cases} 5 \text{ arrays}, & N = 2, \\ 15 \text{ arrays}, & N = 3. \end{cases} \tag{18}$$

Because the total number of arrays needed to store all components of displacement, velocity, acceleration, stress and strain, in addition to the medium properties, is of the order of 15 in 2-D and 25 in 3-D, it can be seen that the additional memory cost of the tensorial formulation is important, particularly in 3-D, and constitutes the main drawback to

the use of this approach. This cost would not be reduced if only horizontal curved grid lines were used (keeping purely vertical grid lines) because no components of the metric tensor would vanish, as can be seen in its expression in terms of the partial derivatives of the grid transformation functions (see Appendix A). The way to save memory could be to use orthogonal grids for which the off-diagonal terms of the metric tensor equal zero, but such grids are difficult to generate, particularly in 3-D (Ryskin & Leal 1983).

GRID GENERATION, METRIC AND CONNECTION CALCULATION

Consider a geological model specified as a set of points defining curved interfaces between layers and a curved free surface. In Appendix B, using an interpolation algorithm based on the third-degree Hermite polynomials, we describe a simple approach to generate a grid whose 'horizontal' lines follow the interfaces, and whose 'vertical' lines have given tangent vectors to the interfaces, as illustrated in Fig. 1.

It is then possible to define an analytic transformation function from a square computational domain (ξ, η) to the physical space $\vec{r} = (x, z)$, and hence the coordinate transformation functions $x = x(\xi, \eta)$ and $z = z(\xi, \eta)$.

To obtain a high precision for the numerical boundary conditions at interfaces and the free surface, it is frequently necessary to refine the grid in the vicinity of these interfaces (Jastram & Behle 1992; Rodrigues & Mora 1992). The grid generation approach used has the useful property that the grid can be refined or stretched close to the boundaries of a layer, hence allowing an increase in the number of grid points close to the interfaces and the free surface, and a decrease in the number of grid points close to an absorbing boundary.

With a knowledge of the transformation functions $x = x(\xi, \eta)$ and $z = z(\xi, \eta)$ from the computational domain to the physical space, the basis vectors of the natural frame associated with a point whose position is $\vec{M}$ are given by

$$\vec{e}_i = \frac{\partial \vec{M}}{\partial \xi^i} = \frac{\partial x^j}{\partial \xi^i} \vec{e}'_j, \tag{19}$$

with $x^j \in \{x, z\}$ and $\xi^i \in \{\xi, \eta\}$, $\vec{e}'_j$ being the basis vectors of

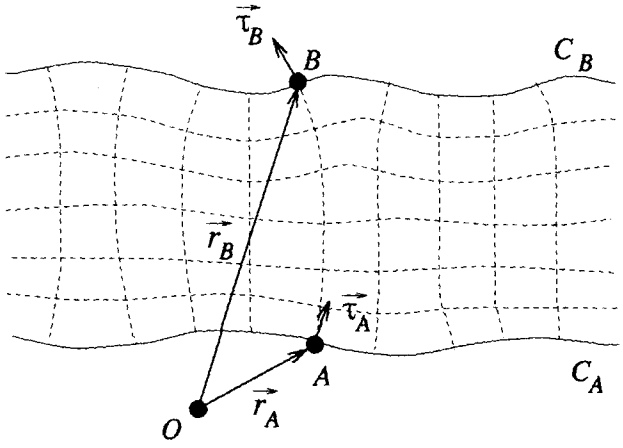

Figure 1. The grid generation process seeks a curve linking points A and B with known tangent vectors $\vec{\tau}_A$ and $\vec{\tau}_B$. These tangent vectors can, for instance, correspond to the normals at positions A and B of two curved interfaces denoted C_A and C_B which bound a given layer.

a Cartesian orthonormal frame. This means that the metric tensor in a Euclidian space (i.e. flat space) is given by

$$g_{ij} = \vec{e}_i \cdot \vec{e}_j = \frac{\partial x^k}{\partial \xi^i} \vec{e}'_k \cdot \frac{\partial x^l}{\partial \xi^j} \vec{e}'_l = \frac{\partial x^k}{\partial \xi^i} \frac{\partial x^l}{\partial \xi^j} \delta_{kl}, \tag{20}$$

as $\vec{e}'_k \cdot \vec{e}'_l = \delta_{kl}$ in the Cartesian orthonormal frame.

This expression allows g_{ij} and g^{ij} to be calculated in terms of the partial derivatives of the transformation functions (see also Appendix A). As the functions $x_i = x_i(\xi, \eta)$ are known analytically, it would be possible to calculate the metric tensor g_{ij} using the analytic expressions for the partial derivatives of the transformation functions. The metric tensor can also be calculated numerically using the same discrete spatial derivative operator as the one used to solve the wave equation (in our case a Chebyshev operator). Although it may seem surprising, the work of Thompson *et al.* (1985) has shown that the second approach leads to a lower global numerical error when calculating spatial derivatives in the curved domain. For this reason, we have chosen to compute the metric tensor using the numerical approach. The same discrete derivative operators are subsequently applied to the components of g_{ij} to obtain the Christoffel symbols using eq. (9).

NUMERICAL ALGORITHM

We use a Chebyshev operator (see for instance Carcione 1994) to solve the tensorial wave equation. The variables are discretized on a grid defined on $[-1, 1] \times [-1, 1]$ by the Gauss–Lobatto–Chebyshev points. The fields are expanded in terms of a finite sequence of orthogonal functions which are the Chebyshev polynomials. Time extrapolation is performed using an explicit fourth-order Runge–Kutta scheme, which gives a favourable stability condition for $dt = O(N^{-1})$, where N is the number of grid points in each direction of the computational grid. The Chebyshev algorithm has been chosen mainly because it is free of numerical dispersion up to the Nyquist frequency, and also because boundary conditions, for instance the free-surface condition, can be implemented in a straightforward and efficient way. Because the purpose of this paper is mainly to introduce and validate the tensorial formulation of the wave equation, we do not present the Chebyshev algorithm in detail here. The reader can refer to the very precise description given in Carcione & Wang (1993).

Tests were also done using a non-staggered finite-difference method, but the algorithm yielded numerical artefacts in the case of high velocity contrasts at an interface, due to the fact that the non-staggered grid is in fact composed of two weakly coupled staggered grids (Magnier, Mora & Tarantola 1994). This approach has therefore been abandoned. Staggered finite-difference algorithms are not well suited to the curved formulations of the wave equation (tensorial or chain rule), due to the fact that numerous interpolations are needed at each time step, thus reducing the accuracy of the scheme and adding significantly to the computational cost. Interpolations are required on a staggered grid in the tensorial formulation in order to compute a covariant derivative, which requires the sum, at a given grid point, of a partial derivative of the field and Christoffel symbols multiplied by the field itself. Note that the chain rule approach on a staggered grid also requires interpolations to compute the Cartesian derivatives, as derivatives computed along different axes have to be summed at the same grid point.

In the case of a force acting at a point, the source term $\vec{\varphi}$ of the wave equation (5) can be written

$$\vec{\varphi}(\mathbf{x}, t) = \delta(\mathbf{x} - \mathbf{x}_s) f(t - \tau)\vec{n}, \tag{21}$$

where $\delta(\mathbf{x} - \mathbf{x}_s)$ is the Dirac distribution centred on the source point $\mathbf{x}_s$, $f(t)$ is a causal function describing the temporal dependence of the source, τ is the onset time of the source and $\vec{n}$ is a unit vector specifying the direction of the source force. The source term is converted from Cartesian to generalized coordinates using

$$\varphi_\xi = \varphi_x \frac{\partial x}{\partial \xi} + \varphi_z \frac{\partial z}{\partial \xi},$$

$$\varphi_\eta = \varphi_x \frac{\partial x}{\partial \eta} + \varphi_z \frac{\partial z}{\partial \eta}. \tag{22}$$

The time extrapolation scheme is initiated with null conditions $v(\mathbf{x}, t_0) = 0$ and $\sigma(\mathbf{x}, t_0) = 0$, with $t_0 = 0$ denoting the beginning of the simulation. The stability of the scheme is assured by a classical Courant condition:

$$\Delta t \left(\frac{v_P}{\Delta x} \right)_{\max} \leq \varepsilon, \tag{23}$$

where Δx is the distance between grid points in the physical domain, v_P is the P velocity inside the medium and ε is the Courant number.

The scheme is free of numerical dispersion up to the Nyquist frequency. This condition is met by choosing a maximum grid spacing such that the minimum number of grid points per wavelength obeys the relation

$$n_\lambda^{\min} = \frac{1}{f_{\max}} \left(\frac{v_S}{\Delta x} \right)_{\min} \geq n_\lambda^{\text{scheme}}, \tag{24}$$

where Δx is the distance between grid points in the physical domain, v_S is the S wave velocity inside the medium, $f_{\max}$ is the maximum frequency of the source, and $n_\lambda^{\text{scheme}} \geq 2$ is the minimum number of grid points per wavelength that can be accurately modelled by the numerical scheme (~ 4 for a Chebyshev operator).

The boundary conditions are open radiation conditions (absorbing boundaries) at each border of the model except the free surface. These conditions and the free-surface condition are applied in the Chebyshev algorithm by decomposing the wavefield into one-way modes (characteristics) perpendicular to the boundaries, and modifying these modes according to the boundary conditions, as described in detail in Carcione & Wang (1993).

NUMERICAL TESTS IN 2-D

Numerical tests were conducted in 2-D using two different models: the first model to validate the tensorial approach by comparing the results obtained to an analytical solution, and second to demonstrate its ability to model a free surface with topography.

Validation of the tensorial formulation

In order to validate the tensorial method, we compare the results obtained on the tilted Lamb problem to the analytical solution. The grid used is shown in Fig. 2, and has a size of 187×187. The slope makes an angle of 10° with the horizontal direction. The medium is homogeneous, having a P-wave velocity of 3200 m s^{-1} and an S-wave velocity of 1847.5 m s^{-1}, corresponding to a Poisson's ratio of $\sigma = 0.25$. The density is 1000 kg m^{-3}.

The source is a force having a direction normal to the slope. It is placed at $x_s = 665$ m just below the free surface, at a depth of $z_s = 8$ m. One receiver (R1) is placed on the free surface at $x_{R1} = 1793.3$ m. Another receiver (R2) is placed in the model at $x_{R2} = 1028.9$ m at a depth of $z_{R2} = 832.5$ m. Thus, the first receiver will record mainly a very strong Rayleigh wave, while the second will record the direct P and direct S waves that propagate in the curved grid. This will allow the tensorial formulation to be validated for the three kinds of waves that propagate in the solid.

Computation proceeded for 2500 time steps with a time step of $\Delta t = 0.35$ ms, leading to a total recording time of 0.875 s. The length of the sides of curvilinear grid cells in the physical domain ranged from $\Delta x_{\min} = 1.4$ m to $\Delta x_{\max} = 16.3$ m along the 'horizontal' grid lines and from $\Delta z_{\min} = 0.9$ m to $\Delta z_{\max} = 14.1$ m along the 'vertical' grid lines. The angle between the horizontal and vertical lines of the grid ranged from $\theta_{\min} = 80.8°$ to $\theta_{\max} = 90.0°$.

The source function was the second derivative of a Gaussian in time, with a central frequency $f_0 = 20.0$ Hz and a maximum frequency of $f_{\max} = 50.0$ Hz (defined as the frequency where the amplitude spectrum is 5 per cent of the maximum value). The minimum number of grid points per fundamental wavelength (corresponding to the biggest grid cells) was 9.7 for the P wave and 5.6 for the S wave.

Snapshots of the velocity vector are presented in Fig. 3, showing the direct P wave, the direct S wave and a strong Rayleigh wave that propagates along the slope. The seismograms recorded at the two receivers are shown in Fig. 4. A very good agreement is found between the analytical solution and the numerical results, both for the strong Rayleigh wave (at receiver R1) and for the body waves (at receiver R2), thus validating the tensorial approach for the elastic wave equation.

Simulation with a free-surface topography

To test the capability of the tensorial approach to model a free-surface topography, we conducted two simulations in the model shown in Fig. 5. The grid has 187×187 points. A two-layer model was used, the interface having a curved shape. In the upper layer, the density was set to 1000 kg m^{-3}, the P-wave velocity to 2800 m s^{-1}, and the S-wave velocity to 1820 m s^{-1}, corresponding to a Poisson's ratio of $\sigma = 0.13$. In the lower layer, the density was set to 1500 kg m^{-3}, the P-wave velocity to 3800 m s^{-1}, and the S-wave velocity to 2000 m s^{-1}, corresponding to a Poisson's ratio of $\sigma = 0.30$. Thus, this two-layer model presents a strong contrast both in velocity and in Poisson's ratio, allowing us to validate the method for realistic geological models. The parameters of the source remain the same as in the tilted Lamb problem.

The length of the sides of the curvilinear grid cells in the physical domain ranges from $\Delta x_{\min} = 1.4$ m to $\Delta x_{\max} = 18.6$ m along the 'horizontal' grid lines and from $\Delta z_{\min} = 2.0$ m to $\Delta z_{\max} = 15.6$ m along the 'vertical' grid lines. The angle between the horizontal and vertical lines of the grid ranges from $\theta_{\min} = 51.7°$ to $\theta_{\max} = 126.5°$.

As the grid is curvilinear, a straight line in the physical domain (e.g. a line of receivers) does not correspond to a

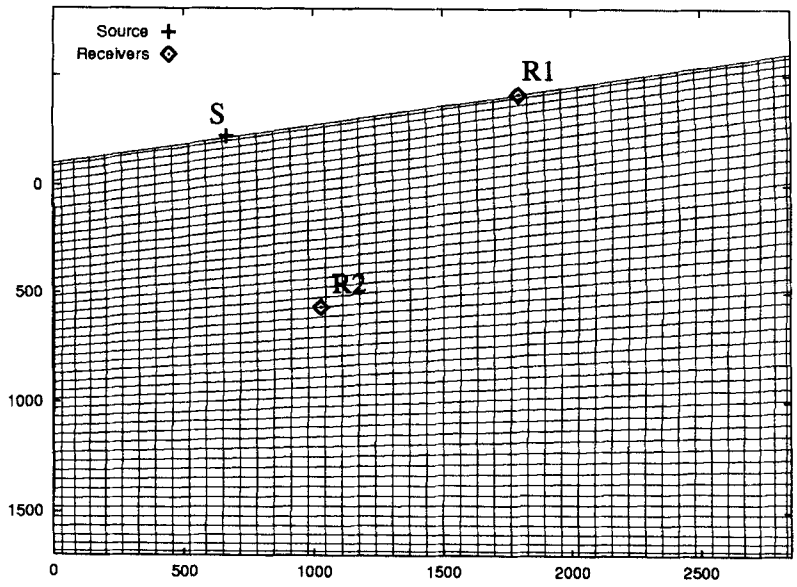

Figure 2. The grid used to validate the tensorial approach with respect to the analytical solution of the tilted Lamb problem. The slope makes an angle of 10° with the horizontal direction. The grid size is 187 × 187. Every fourth grid line is plotted.

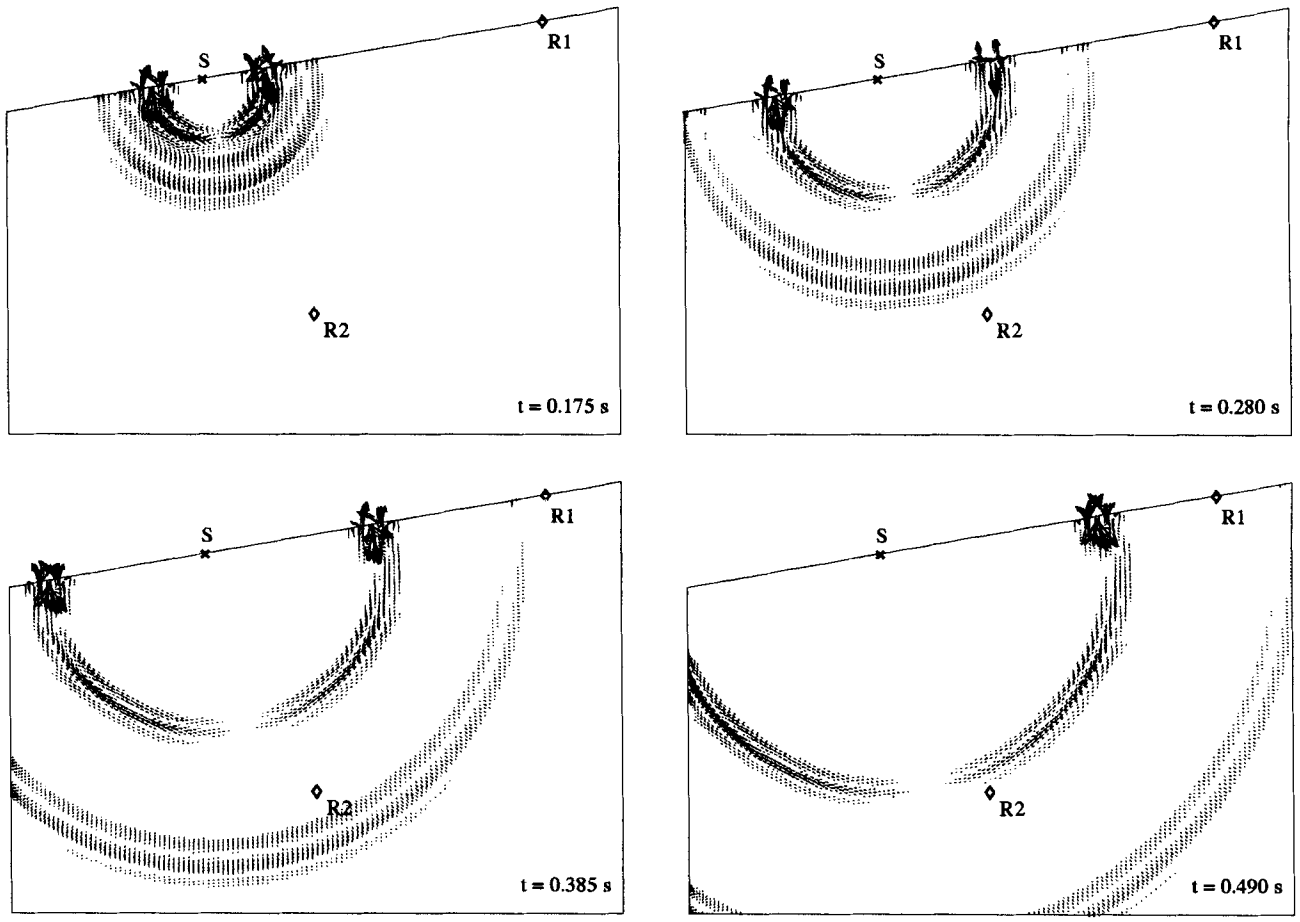

Figure 3. Snapshots of the velocity vector obtained for the tilted Lamb problem with a slope of 10° (see Fig. 2). The cross marks the source position, the diamonds represent the two receivers. The source is a force normal to the slope, placed just below the free surface. One can observe the direct *P* wave, the direct *S* wave and the strong Rayleigh wave that propagates along the slope.

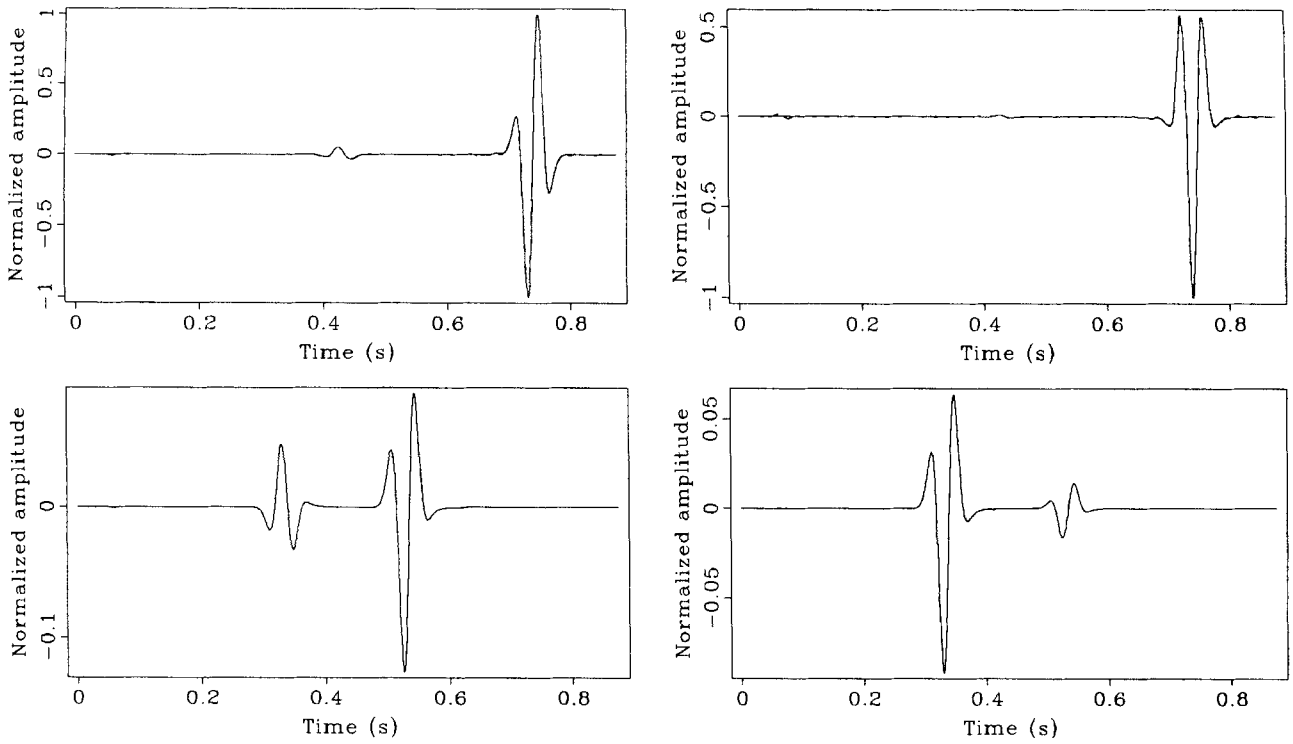

Figure 4. Seismograms of the horizontal component of velocity v_x (left) and the vertical component of velocity v_z (right) for the tilted Lamb problem of Fig. 3. The analytical solution is plotted as a solid line, and the numerical solution obtained with the tensorial formulation as a dashed line. The upper seismograms correspond to the receiver located just below the free surface (R1), and the lower ones to the receiver located at depth (R2). The agreement is almost perfect, the maximum difference being less than 1 per cent.

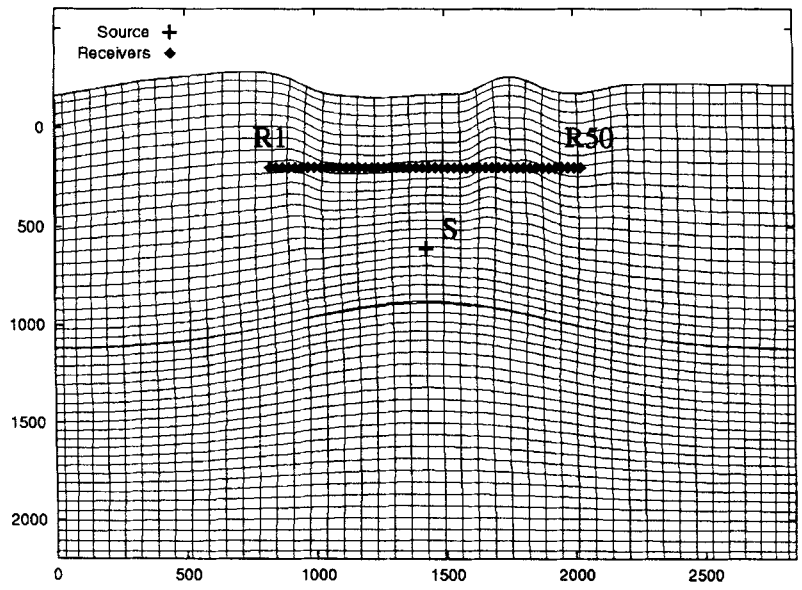

Figure 5. The structure used to test the ability of the tensorial approach to model free-surface topography. The grid size is 187 × 187. Every fourth grid line is plotted.

straight line in the (ξ, η) domain. Consequently, receivers are generally not located at grid points and it is necessary to interpolate the velocity field that is to be recorded on the seismograms. This is achieved using a bilinear interpolation of the field from its known values at the corners of the appropriate grid cell.

As before, the computation proceeded for 2500 time steps with a time step of $\Delta t = 0.35$ ms, leading to a total recording time of 0.875 s. The minimum number of grid points per fundamental wavelength (corresponding to the biggest grid cells) was 7.5 for the P wave and 4.9 for the S wave for these two tests.

Reflected and converted waves in the presence of a surface topography

A vertical force source was located at $x_s = 1425$ m and a depth of $z_s = 776.2$ m from the free surface. 50 equally spaced receivers were placed along a horizontal line between $x_r = 825$ m and $x_r = 2025$ m at a depth of $z_r = 200$ m.

Snapshots are presented in Fig. 6 and seismograms in Fig. 7. The shape of P and S waves reflected by the bumpy free surface is complex and triplications occur (see the reflection from the rightmost hill). Mode conversions of waves reflected at the free surface (P to S and S to P) as well as at the interface between the two layers are also clearly visible.

These results illustrate that the tensorial approach is capable of modelling reflection and conversion of P and S waves at a free surface having a topography, even for a geological model containing strong contrasts of velocity and Poisson's ratio.

The Rayleigh wave

The vertical force source is now located at $x_s = 660.9$ m just below the free surface (at a depth of 10 m). The corresponding snapshots are presented in Fig. 8 and the seismograms in Fig. 9. The direct P and direct S waves are visible in the snapshots as well as a strong Rayleigh wave that propagates along the free surface with a speed slightly slower than that of the S wave.

One can observe an event that is interpreted to be a mode conversion from a Rayleigh wave to a body wave in a region where the free-surface topography changes abruptly on the leftmost bump (see snapshots at $t = 0.280$ s and $t = 0.350$ s). The energy converted from the Rayleigh to a body wave appears as a localized body-wave event that trails just after the direct S wave. This event appears to 'peel off' as the Rayleigh wave follows the concave portion of the bump. This event can also

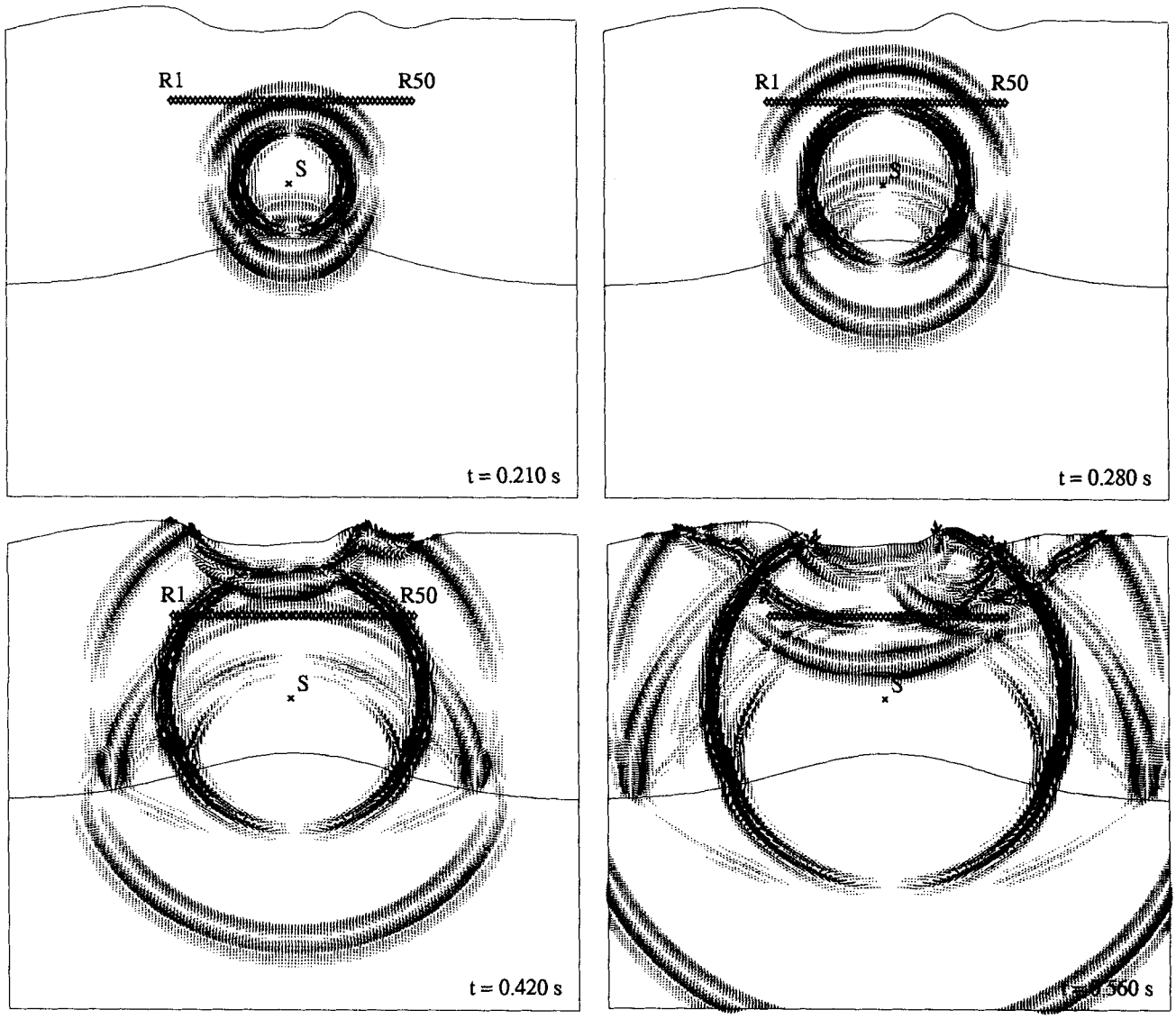

Figure 6. Snapshots of the velocity vector obtained for a model with a non-flat free-surface topography (see Fig. 5). The cross marks the source position, the row of diamonds represents the line of receivers. The source is a vertical force placed in the model at a depth of $z_s = 776.2$ m. One can observe the complex shapes of the waves, for example triplications that occur after reflection on the rightmost hill. Strong reflected waves are generated at the interface between the two media.

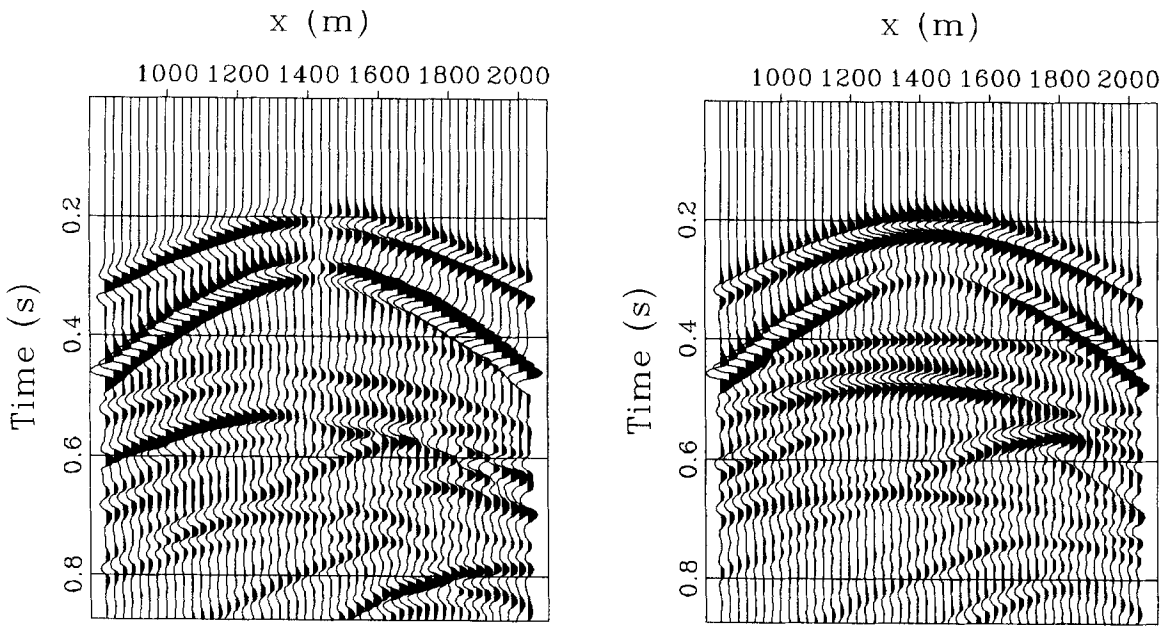

Figure 7. Seismograms of the horizontal component of the velocity v_x (left) and of the vertical component v_z (right) for the model with free-surface topography (Fig. 5). The source is a vertical force in the model at a depth of $z_s = 776.2$ m and the receiver line is located inside the medium.

be clearly seen on the horizontal component v_x of the velocity recorded at the free surface in the seismograms of Fig. 9. The existence of such Rayleigh to body wave mode conversions is in agreement with the results of Jih, McLaughlin & Der (1988), who also observed similar events in their numerical experiments when Rayleigh waves encountered abrupt changes in the free-surface topography. Furthermore, this phenomenon has been demonstrated in the theoretical study of Rulf (1969) for Rayleigh waves travelling along curved surfaces.

These results demonstrate that the tensorial formulation is capable of modelling Rayleigh waves in the presence of free-surface topography.

CONCLUSIONS

It is advantageous to have the ability to solve the wave equation directly in curved grids whose lines match geological interfaces and the free surface. This leads to more precise solutions of sharp curved interface models than are possible using Cartesian grid methods.

A tensorial formulation is presented that enables the wave equation to be solved directly on a curved grid without the need to introduce a Cartesian coordinate system. Such an approach is more natural than the widely used chain rule method that solves the wave equation written in Cartesian coordinates by making use of the chain rule to express the spatial derivatives in terms of those computed in the curved grid. Furthermore, the tensorial approach can be implemented more efficiently than the chain rule method as it requires computation of the same number of discrete spatial derivatives as the Cartesian case.

A simple algebraic grid generation procedure yields grids whose lines follow the different interfaces and that become controllably finer as interfaces are approached. This allows the method to be free of the numerical artefacts that would result from the staircase discretization of the interfaces in the Cartesian case.

Numerical tests using a Chebyshev algorithm in 2-D are used to validate the tensorial approach and to illustrate its capability to model curved interfaces as well as free-surface topography. For the tilted Lamb problem, an excellent agreement is found with the analytical solution. For the case of a model having surface topography, complex shapes of the different waves, such as triplications, are observed. In addition, if the source is close enough to the surface, mode conversions between Rayleigh and body waves are observed when bumps on the free surface are encountered.

Additional research is required to improve the grid generation methodology, to study whether it is possible to adapt the approach to the case of non-smooth curved surfaces (i.e. models with pinchouts etc.), and to extend the algorithm to the 3-D case.

ACKNOWLEDGMENTS

The authors would like to thank José Carcione, Dominique Rodrigues, Albert Tarantola, Christophe Doursat and Emmanuel Dormy for very fruitful discussions.

This research has been funded in part by the French Ministry of Education and Research and the National Center for Scientific Research (CNRS). It could not have been done without the support of the sponsors of the Seismic Simulation Project (Amoco, Laboratoire de Géophysique, Elf Aquitaine, GOCAD and Shell).

Computations were performed using the Connection Machine CM5 of the French National Centre for Parallel Computing in Earth Sciences (CNCPST) and the Cray J90 of the Centre de Calcul et Réseaux (CCR).

REFERENCES

Brillouin, L., 1964. *Tensors in Mechanics and Elasticity,* Academic Press, New York, NY.

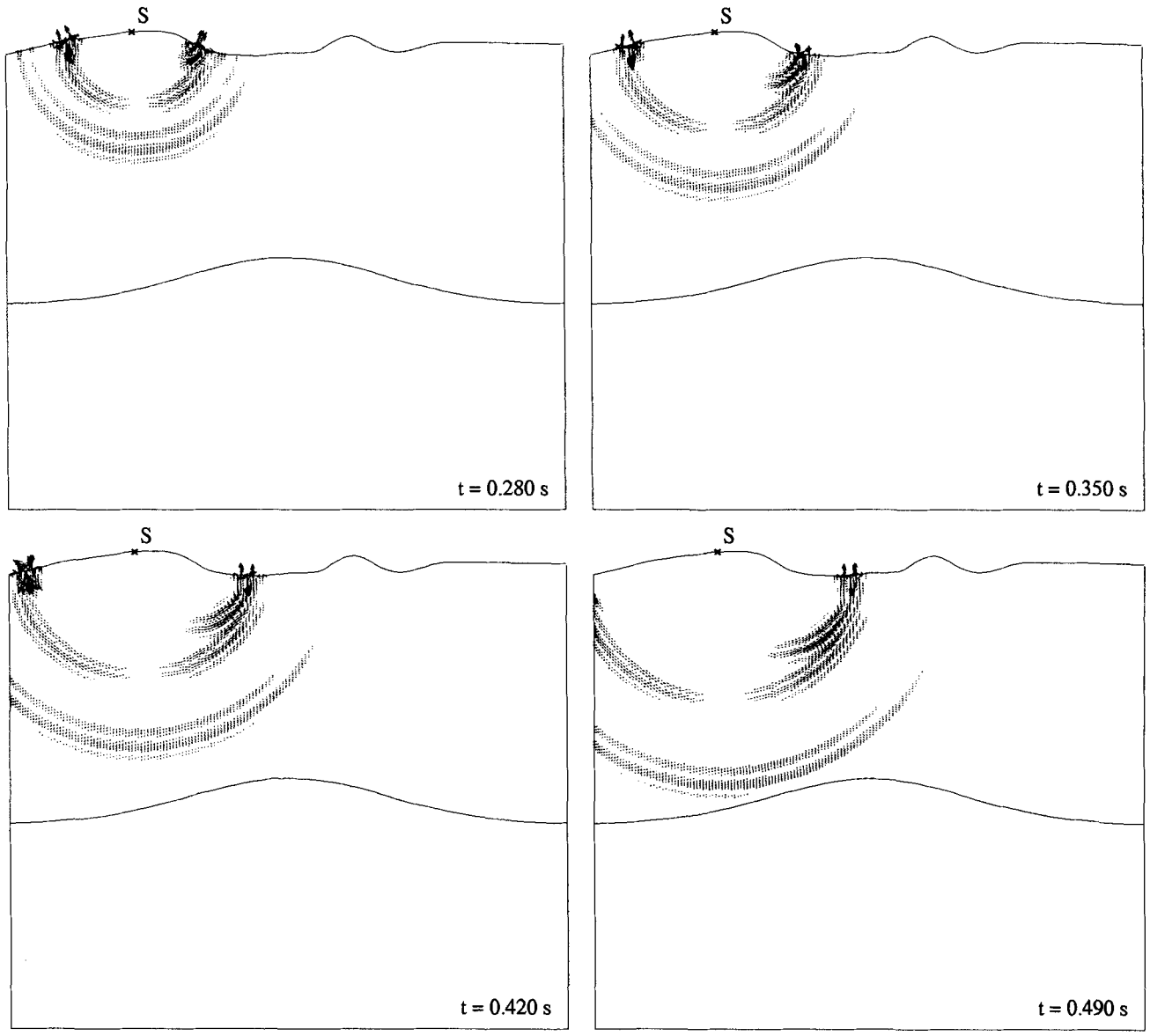

Figure 8. Snapshots of the velocity vector obtained for a model with a non-flat free-surface topography (see Fig. 5). The cross marks the source position. The source is a vertical force placed just below the free surface. One can observe the propagation of a strong Rayleigh wave along the curved surface, as well as a mode conversion from a Rayleigh to body wave when the Rayleigh wave encounters a strong curvature of the free surface on the leftmost bump.

Carcione, J.M., 1994. The wave equation in generalized coordinates, *Geophysics,* **59,** 1911–1919.

Carcione, J.M. & Wang, J.P., 1993. A Chebyshev collocation method for the elastodynamic equation in generalized coordinates, *Comp. Fluid Dyn. J.,* **2,** 269–290.

Fletcher, C.A.J., 1991. *Computational Fluid Dynamics,* Springer Verlag, New York, NY.

Fornberg, B., 1988. The pseudospectral method: accurate representation of interfaces in elastic wave calculations, *Geophysics,* **53,** 625–637.

Hestholm, S. & Ruud, B., 1994. 2D finite-difference elastic wave modeling including surface topography, *Geophys. Prospect.,* **42,** 371–390.

Jastram, C. & Behle, A., 1992. Acoustic modeling on a grid of vertically varying spacing, *Geophys. Prospect.,* **40,** 157–169.

Jih, R.S., McLaughlin, K.L. & Der, Z.A., 1988. Free-boundary conditions of arbitrary polygonal topography in a two-dimensional explicit elastic finite-difference scheme, *Geophysics,* **53,** 1045–1055.

McConnell, A.J., 1957. *Applications of Tensor Analysis,* Dover Publications, New York, NY.

Magnier, S.A., Mora, P. & Tarantola, A., 1994. Finite differences on minimal grids, *Geophysics,* **59,** 1435–1443.

Muir, F., Dellinger, J., Etgen, J. & Nichols, D., 1992. Modelling elastic fields across irregular boundaries, *Geophysics,* **57,** 1189–1193.

Nielsen, P., If, F., Berg, P. & Skovgaard, O., 1994. Using the pseudo-spectral technique on curved grids for 2D acoustic forward modeling, *Geophys. Prospect.,* **42,** 321–341.

Nielsen, P. & Skovgaard, O., 1990. The effect of using non-orthogonal boundary-fitted grids for solving the shallow water equations, *Int. J. Num. Meth. Fluids,* **11,** 177–188.

Rodrigues, D. & Mora, P., 1992. Analysis of a finite difference solution to 3D elastic wave propagation, in *Expanded Abstracts Soc. Expl. Geophys.,* 62nd Int. Mtg, pp. 1247–1250, SEG, Tulsa, OK.

Rulf, B., 1969. Rayleigh waves on curved surfaces, *J. acoust. Soc. Am.,* **45,** 493–499.

Ryskin, G. & Leal, L.G., 1983. Orthogonal mapping, *J. comput. Phys.,* **50,** 71–100.

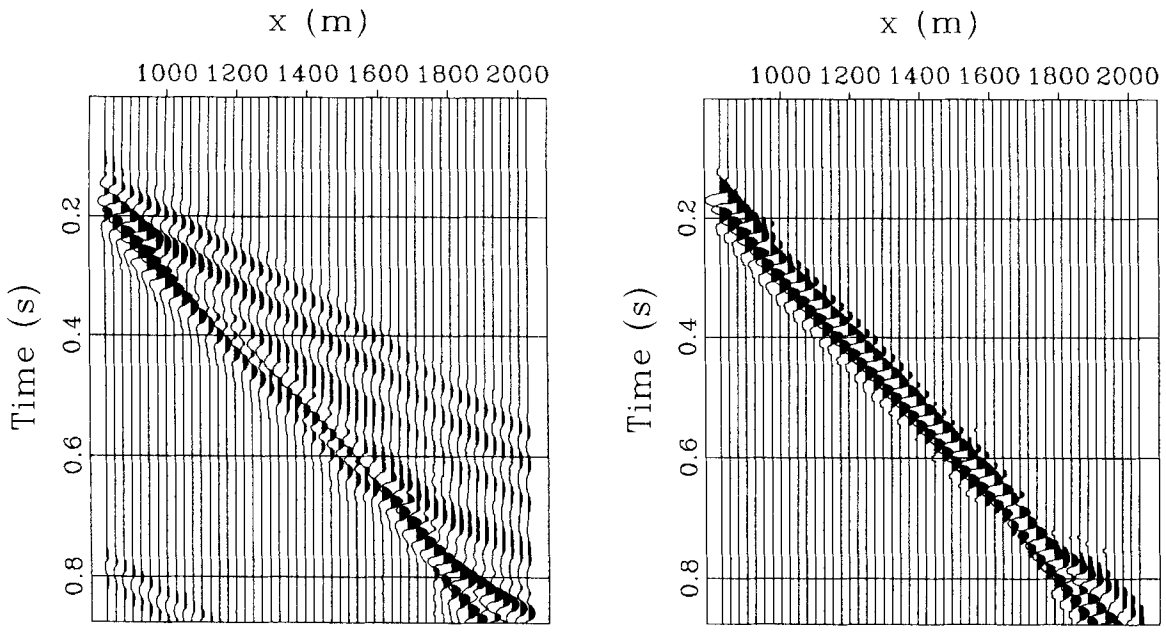

Figure 9. Seismograms of the horizontal component of the velocity v_x (left) and of the vertical component v_z (right) for the model with free-surface topography (Fig. 5). The source is a vertical force located just below the free surface. The receiver line is placed on the free surface. One can observe a strong Rayleigh wave that propagates along the surface, as well as mode conversions from a Rayleigh to body wave which appear clearly on the horizontal component. The small-amplitude event on the horizontal component at $t = 0.8$ s is the reflection from the interface.

Spain, B., 1965. *Tensor Calculus,* John Wiley & Sons, New York, NY.

Tessmer, E. & Kosloff, D., 1994. 3-D elastic modeling with surface topography by a Chebyshev spectral method, *Geophysics,* **59,** 464–473.

Tessmer, E., Kosloff, D. & Behle, A., 1992. Elastic wave propagation simulation in the presence of surface topography, *Geophys. J. Int.,* **108,** 621–632.

Thompson, J.F., Warsi, Z.U.A. & Mastin, C.W., 1985. *Numerical Grid Generation—Foundations and Applications,* North Holland Publishing Co, New York, NY.

Virieux, J., 1986. P–SV wave propagation in heterogeneous media: velocity–stress finite-difference method, *Geophysics,* **51,** 889–901.

APPENDIX A: BASIC RULES FOR TENSORIAL FORMULATION

Scalars and vectors are particular cases of more general quantities, called *tensors*, which are transformed according to a linear and homogeneous transformation when changing between two systems of curvilinear coordinates. Changing from $\{x^i\}$ to $\{x'^i\}$, for example, we have the transformation relation for a tensor of order $p+q$ (see, for example, Spain 1965)

$$A_{j_1 \dots j_q}{}^{i_1 \dots i_p} = \frac{\partial x^{l_1}}{\partial x'^{j_1}} \cdots \frac{\partial x^{l_q}}{\partial x'^{j_q}} \frac{\partial x'^{i_1}}{\partial x^{k_1}} \cdots \frac{\partial x'^{i_p}}{\partial x^{k_p}} A_{l_1 \dots l_q}{}^{k_1 \dots k_p}, \tag{A1}$$

where $i_1, \dots, i_p$ are called *contravariant* indices and $j_1, \dots, j_q$ are called *covariant* indices. For instance, the transformation law from a Cartesian to a curvilinear frame for a covariant tensor of order one such as velocity is

$$v_\xi = v_x \frac{\partial x}{\partial \xi} + v_z \frac{\partial z}{\partial \xi}, \tag{A2}$$

$$v_\eta = v_x \frac{\partial x}{\partial \eta} + v_z \frac{\partial z}{\partial \eta},$$

and for a symmetric covariant tensor of order two such as stress it is

$$\sigma_{\xi\xi} = \sigma_{xx} \left(\frac{\partial x}{\partial \xi} \right)^2 + \sigma_{zz} \left(\frac{\partial z}{\partial \xi} \right)^2 + 2\sigma_{xz} \frac{\partial x}{\partial \xi} \frac{\partial z}{\partial \xi},$$

$$\sigma_{\eta\eta} = \sigma_{xx} \left(\frac{\partial x}{\partial \eta} \right)^2 + \sigma_{zz} \left(\frac{\partial z}{\partial \eta} \right)^2 + 2\sigma_{xz} \frac{\partial x}{\partial \eta} \frac{\partial z}{\partial \eta},$$

$$\sigma_{\xi\eta} = \sigma_{\eta\xi} = \sigma_{xx} \frac{\partial x}{\partial \xi} \frac{\partial x}{\partial \eta} + \sigma_{zz} \frac{\partial z}{\partial \xi} \frac{\partial z}{\partial \eta} + \sigma_{xz} \left(\frac{\partial x}{\partial \xi} \frac{\partial z}{\partial \eta} + \frac{\partial x}{\partial \eta} \frac{\partial z}{\partial \xi} \right). \tag{A3}$$

To transform from the contravariant to the covariant formulation, or from the covariant to the contravariant formulation, one can write

$$A_{i_1 \dots i_p} = g_{i_1 j_1} \dots g_{i_p j_p} A^{j_1 \dots j_p}, \qquad A^{i_1 \dots i_p} = g^{i_1 j_1} \dots g^{i_p j_p} A_{j_1 \dots j_p}, \tag{A4}$$

where g_{ij} is the metric tensor in the covariant formulation and g^{ij} is the metric tensor in the contravariant formulation. The metric tensor is symmetric by definition ($g_{ij} = g_{ji}$). This tensor g_{ij} can be obtained from the partial derivatives of the (known) direct transformations $x_i = x_i(\xi_1, \dots, \xi_n)$ (see eq. 20). For example, in 2-D, let $x_\xi, x_\eta, z_\xi, z_\eta$ be the partial derivatives of the direct transformation between the two systems of coordinates. Then we can write

$$g_{11} = x_\xi^2 + z_\xi^2, \qquad g_{22} = x_\eta^2 + z_\eta^2,$$

$$g_{12} = g_{21} = x_\xi x_\eta + z_\xi z_\eta. \tag{A5}$$

The Jacobian of the transformation is defined by

$$J = (x_\xi z_\eta - x_\eta z_\xi)^{-1}. \tag{A6}$$

The partial derivatives of the inverse transformation can then be obtained, even if the inverse transformation itself

$\xi_i = \xi_i(x, z)$ is not known analytically (but exists, meaning that the Jacobian never equals zero), by writing

$$\xi_x = Jz_\eta, \qquad \xi_z = -Jx_\eta,$$
$$\eta_x = -Jz_\xi, \qquad \eta_z = Jx_\xi. \tag{A7}$$

The expression for the metric tensor in contravariant formulation is then

$$g^{11} = \xi_x^2 + \xi_z^2, \qquad g^{22} = \eta_x^2 + \eta_z^2,$$
$$g^{12} = g^{21} = \xi_x\eta_x + \xi_z\eta_z \tag{A8}$$

The Christoffel symbols of the second kind that appear in the expression for the covariant derivative are *not* tensors, as they do not follow the transformation law given by eq. (A1), but are symmetric in the lower indices:

$$\Gamma_{ij}^{\ k} = \Gamma_{ji}^{\ k}. \tag{A9}$$

APPENDIX B: GRID GENERATION PROCESS

If we consider two points A and B belonging to the curved interfaces C_A and C_B, respectively, that bound a given layer, a curve linking A to B can be constructed with given unit tangent vectors $\vec{\tau}_A$ at A and $\vec{\tau}_B$ at B (see Fig. 1), as

$$\vec{r}(\eta^*) = \alpha_0^0(\eta^*)\vec{r}_A + \alpha_1^0(\eta^*)\vec{r}_B + \alpha_0^1(\eta^*)h_0\vec{\tau}_A + \alpha_1^1(\eta^*)h_1\vec{\tau}_B, \tag{B1}$$

where $\eta^* \in [0, 1]$ and α_i^j are the four third-degree Hermite polynomials (see Fig. B1) defined as

$$\alpha_0^0(\eta^*) = 1 - 3\eta^{*2} + 2\eta^{*3},$$
$$\alpha_1^0(\eta^*) = 3\eta^{*2} - 2\eta^{*3},$$
$$\alpha_0^1(\eta^*) = \eta^* - 2\eta^{*2} + \eta^{*3},$$
$$\alpha_1^1(\eta^*) = -\eta^{*2} + \eta^{*3}, \tag{B2}$$

where $\vec{r}$ denotes the position vector along the curve. The two constants h_0 and h_1 define the length of the tangent vectors and will be used in the following to define the size of the grid cells close to the boundaries.

The algebraic mapping method described above—see Fletcher (1991)—uses the properties of the third-degree Hermite polynomials (see Fig. B1) and their first derivatives (see Fig. B2) to ensure that the required conditions are met.

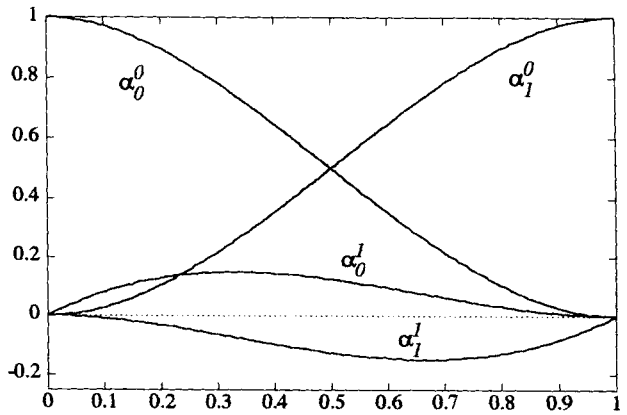

Figure B1. The four third-degree Hermite polynomials that are used to generate a curved grid.

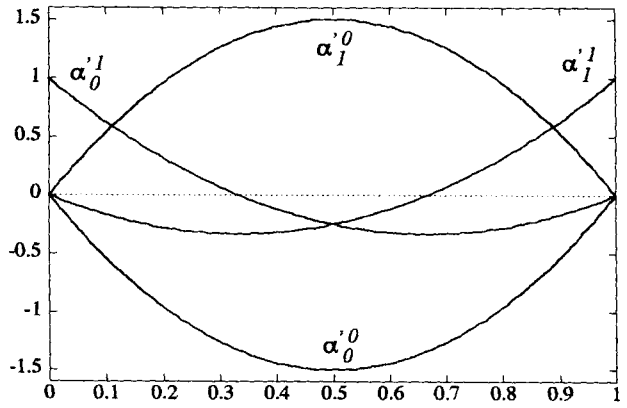

Figure B2. The first derivatives of the third-degree Hermite polynomials that are used to generate a curved grid.

This is easy to verify by calculating the tangent to this curve,

$$\vec{\tau}(\eta^*) = \frac{\partial\vec{r}(\eta^*)}{\partial\eta^*} = a_0'^0(\eta^*)\vec{r}_A + \alpha_1'^0(\eta^*)\vec{r}_B + \alpha_0'^1(\eta^*)h_0\vec{\tau}_A + \alpha_1'^1(\eta^*)h_1\vec{\tau}_B, \tag{B3}$$

and applying eqs (B1) and (B3) at points A and B, which yields $\vec{r}(0) = \vec{r}_A$, $\vec{r}(1) = \vec{r}_B$, $\vec{\tau}(0) = h_0\vec{\tau}_A$ and $\vec{\tau}(1) = h_1\vec{\tau}_B$ as desired.

We can extend this method to generate a 2-D grid within a layer bounded by curved interfaces. Consider a square grid in the (ξ, η) domain with $\xi \in [0, 1, \ldots, N_\xi]$ and $\eta \in [0, 1, \ldots, N_\eta]$. The corresponding curved grid is defined by

$$\vec{r}(\xi, \eta) = \alpha_0^0(\eta^*)\vec{r}_A(\xi) + \alpha_1^0(\eta^*)\vec{r}_B(\xi) + \alpha_0^1(\eta^*)h_0\vec{\tau}_A(\xi) + \alpha_1^1(\eta^*)h_1\vec{\tau}_B(\xi), \tag{B4}$$

where

$$\eta^* = \frac{\eta}{N_\eta}. \tag{B5}$$

In eq. (B4), $\vec{r}_A(\xi)$ and $\vec{r}_B(\xi)$ specify the set of departure and arrival points of the grid lines on the upper and lower interfaces respectively, and $\vec{\tau}_A(\xi)$ and $\vec{\tau}_B(\xi)$ the corresponding tangents at these points. This equation constitutes an analytic trans-

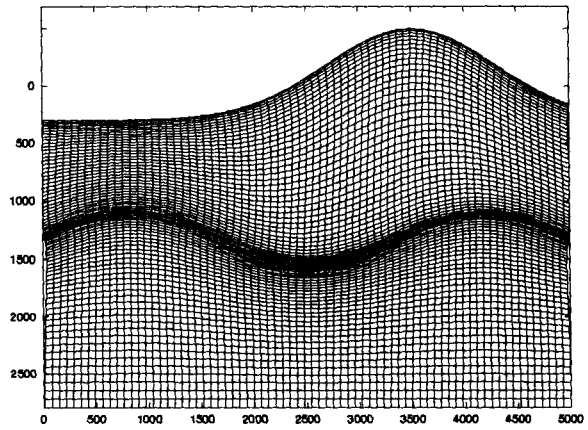

Figure B3. Example of a grid generated with the algebraic method. The use of Hermite polynomials has lead to a grid that becomes finer as the interfaces are approached. Note that the left and right boundaries are distorted and not perfectly vertical.

formation function from the square computational domain (ξ, η) to the physical space $\vec{r} = (x, z)$. Hence, it defines the coordinate transformation functions $x = x(\xi, \eta)$ and $z = z(\xi, \eta)$.

The grid generation approach described above has the useful property that the grid can be refined or stretched close to the boundaries of a layer by specifying appropriate values of h_0 and h_1 to define the length of the vectors normal to an interface. This can be demonstrated by developing (B1) to the first order in η^* close to $\eta^* = 0$ and $\eta^* = 1$, respectively, yielding $\|\Delta\vec{r}\| \simeq h_0 \Delta\eta^*$ and $\|\Delta\vec{r}\| \simeq h_1 \Delta\eta^*$, where $\|\Delta\vec{r}\|$ represents the change in position in the physical domain for a given change $\Delta\eta^*$ in the computational domain. Hence, the sizes of the grid cells close to the lower and upper boundaries are respectively $h_0 \Delta\eta^*$ and $h_1 \Delta\eta^*$.

An example of a grid obtained by this algebraic method for a two-layer model with surface topography is shown in Fig. B3. The grid becomes finer as the interfaces are approached, except at the bottom of the grid which corresponds to the absorbing boundary. The grid size is 512×512 and the values of the two constants are $h_0 = 500$ and $h_1 = 500$ in the upper layer, and $h_0 = 2850$ and $h_1 = 500$ in the lower layer.